

# Final Project Report

Riku Ito, Agustin Loureiro, Joseph Letteny, James Wareham, Sathvik Ramanan

## I. PROJECT IDEA & PURPOSE

Inflatable soft robots have been researched in a variety of applications - most notably in wearables, however, their advantages of being soft, conformable and able to cover large distances per stroke create untapped opportunities for transport in challenging environments meriting further research. The primary objective of this work is to develop a robot made entirely of soft materials capable of walking, active steering, passive steering with conformity to its surroundings, and carrying devices to accomplish other functions such as grasping.

We fabricated a robot body using folded paper contained in a TPE film pouch. The primary actuation along the body of the robot relies on inflating and deflating the pouch to extend and compress the folded paper. On each end of the robot, a “foot” was added using an angular pouch motor. Movement can be summarized as a synchronized cycle of lifting one foot, extending the robot body, dropping the foot, lifting the other foot, and compressing the body.

We aimed to characterize the robot in the following ways: force delivered by body actuator stroke to test the robot’s abilities to carry or drag load, force of angular pouch stroke to test maximum foot weight, speed on a flat surface, speed and success of walking on sloped surfaces, and ability to orient to a path carved by curved walls.

We are motivated by the fact that soft, pneumatically actuated robots are particularly suited for navigation in confined, tortuous environments such as pipelines, tunnels, and rubble after disasters. Some of these insights may also translate to work in biological settings where narrow constricted spaces, such as the colon, need to be navigated for surgery or diagnostics. However, biological settings are less applicable within the scope of our research given the size of our manufactured robot.

When combined with application-specific tools (e.g., cameras, gas sensors, probes, micro-grippers, or delivery systems), these robots can perform inspection, diagnosis (e.g. for leaks, mold, blockages), and localized intervention while minimizing the risk of damage to their surroundings and to themselves. Additionally, this research serves as an experimental testbed for studying soft-body locomotion, frictional contact, and novel gait design in soft robotics. We are primarily focused on exploring the locomotion aspect of inflatable soft robots, while recognizing that specific applications will require further engineering to attach and deploy devices of interest.

## II. BACKGROUND & CURRENT RESEARCH

Recent advances in inflatable soft robotics demonstrate how pressurized structures can produce safe, adaptive, and high-deformation behaviors across a wide range of environments. Comoretto et al. show that soft inflatable tubular limbs can self-oscillate using only continuous airflow, generating remarkably fast, autonomous locomotion without electronics [1]. Their work proves that inflatables can serve as both actuators and

structural elements, enabling rapid shape change through internal pressure modulation. Similarly, the SPROUT robot from MIT Lincoln Laboratory relies on an inflatable vine-like body that “grows” via pressurization to navigate rubble voids, demonstrating the power of inflatable robots to access spaces rigid robots cannot [2]. Yet both systems reveal important limitations: the former excels only on open terrain while the latter lacks active gaiting or controlled anchoring—leaving a gap for inflatable robots capable of deliberate, step-based locomotion in confined geometries.

In industrial and pipeline contexts, inflatables also play a central role. The review by Blewitt et al. highlights how many worm-like inspection robots use pneumatically pressurized chambers for radial anchoring and axial extension, validating air-driven peristaltic locomotion as a natural fit for narrow ducts [3]. Guo et al. further extend inflatable design principles with a hollow shell-lattice robot whose deformable pressurized structure allows locomotion in flexible pipelines with flowing fluids—another demonstration that internal pressure can adapt a robot’s body to dynamic, confined environments [4]. However, these inflatable systems still struggle with traction, directional control, navigating irregular surfaces, and maintaining reliable gaiting, illustrating the need for inflatable robots that combine pressurization-based deformation with more robust surface engagement mechanisms—precisely where a flapping-foot system becomes relevant.

In medical and surgical applications, inflatable soft robotics is likewise emerging as a transformative approach. Runciman et al. review the growing use of inflatable, pressure-modulated soft devices for minimally invasive surgery, emphasizing their safety, compliance, and tissue-friendly deformation [5]. Yang et al. demonstrate this approach with a deployable inflatable surgical robot made from thin plastic laminate film and driven by hydraulic pressure via folded-pouch actuators, proving that inflatable robots can be compactly delivered and then expanded into functional geometry inside biological lumens [6]. Yet, like the other inflatable systems, these MIS devices do not provide true locomotion—they inflate to deploy or manipulate but cannot traverse tortuous paths. These limitations across rubble, pipes, and surgical environments motivate the need for an inflatable robot capable of controlled traversal within irregular environments.

Fluid-driven origami-inspired artificial muscles provide promise as an actuation strategy. In a study by Li et al. actuators were built using a zigzag skeleton made of polyether ether ketone (PEEK) contained within a skin of PVC film and actuated via fluid-driven negative pressure [7]. These actuators were fabricated within 10 min, with materials costing less than \$1. Li et al. demonstrated that a FOAM structure weighing 2.6 could lift a 3 kg object within 0.2 s using a -80 kPa vacuum [7]. These results highlight the promises of a FOAM based design: low costs, easy to manufacture and iterate, and high performance in stroke and force output relative to weight. In this study we take

inspiration from this structure and propose it instead as a mechanism for lateral traversal. Combining an accordion body with inflatable angular pouch motors on each end of the body, we aim to create a walking robot with the stroke and power advantages of the FOAM structure and the conformability and adaptability of inflatables in locomotion.

### III. DESIGN & MANUFACTURING

We detail the design and manufacture of four key components of our soft robot: the pneumatically actuated body, the angular pouch feet, steering stiffeners and an inflatable grasper.

#### A. Pneumatically Actuated Body Muscles

The pneumatically actuated body can be classified as a Fluid-driven origami-inspired artificial muscle (FOAM) [7] and contained X layers of folded paper in an accordion like shape and contained within heat welded TPE film. We refer to this as the FOAM accordion body. As air is added the body elongates as the paper accordion is stretched, and as air is removed, the body shrinks as the accordion is compressed.

#### B. Angular Pouch Feet

The first iteration of the angular pouch motors was fabricated from (TPE) film. Each actuator was formed by folding the film into a pocket and heat-welding three sides. A Loctite-coated tube was then inserted into the remaining open edge, and the adhesive created an airtight seal, producing a fully enclosed pouch motor. To improve mechanical output, the pouch motors were installed inside a fabric sleeve. One end of the sleeve was secured to a PLA component featuring a 45° protrusion, while the opposite end was attached to the silicone foot. This configuration provided a rigid reaction surface for the pouches and constrained the relative motion between the foot and PLA structure, allowing the expansion of the pouch motors to more effectively generate angular displacement.

In addition to the TPE-based actuators, one pouch motor was constructed using a heat-weldable fabric. The seams of this actuator were created with a soldering iron, resulting in a significantly stiffer and more robust pouch capable of producing higher and more consistent output forces. The increased stiffness also improved bonding to the fabric sleeve. However, achieving a fully reliable airtight seal using this method proved difficult, and therefore only one fabric-based actuator was incorporated into the final design.

#### C. Steering Stiffeners

Laminar stiffeners were constructed for each side along the length of the robot to aid in active steering. Each stifferener contained 40 sheets of paper contained within heat welded TPE film, similar to the design in Narang et al. [8]. The desired

mechanism of action is to create a vacuum (known as jamming) to stiffen only one side of the robot body during either elongation or compression, causing the robot to reorient toward the jammed or unjammed side, respectively. The stiffeners were attached to the PLA component at either end of the FOAM in order to keep aligned with its orientation while avoiding limiting its actuation.

#### D. Inflatable Grasper

The inflatable grasper was fabricated from TPE film and printer paper. Its operation relies on two distinct components: an outer inflation ring and an inner stiffening ring. During grasping, the outer ring is inflated so that the grasper expands and conforms to the shape of the target object. Once conformity is achieved, the inner ring is stiffened through a laminar jamming mechanism as described by Chen et al [9]. With the stiffening activated, the object can be securely grasped and lifted either with the outer ring inflated or deflated.

To manufacture the grasper, ten sheets of printer paper were cut to 1" × 11" strips and heat-welded into a TPE pouch according to the *Grasper\_Cutout* pattern. A second TPE pouch, empty and without internal paper was also heat-welded and purposefully left attached to the paper-filled pouch. For both pouches, a small opening was left unsealed to allow insertion of actuation tubing.

After welding, the empty TPE pouch was folded inside the paper-lined pouch and temporarily secured with tape to maintain the nested configuration. The ends of each pouch were then taped to themselves to form a ring structure. Finally, actuation tubing was inserted into each pouch and sealed in place using Loctite.

#### E. Assembly of all Components

Assembly of the robot requires the following components:

- Two angular pouch feet
- One central accordion actuator
- Two steering stiffeners
- One inflatable grasper
- One 3D-printed central chassis
- Two 3D-printed pouch motor mounts



Figure X: Full robot assembly.

To begin assembly, one end of the accordion is attached to the central chassis using superglue and allowed to set. The two 3D-printed pouch motor mounts are then glued in place, one at the free end of the accordion and the other at the opposite end of the chassis. Once these structural elements are secured, the steering stiffeners are affixed along their designated attachment points on the motor mounts using tape. The angular pouch feet are then installed by gluing the inflatable side of each foot to its corresponding motor mount and attaching the silicone foot pads to the opposite ends. Finally, the inflatable grasper is superglued inside the central chassis and secured in place, completing the assembly.

#### IV. MODELING

We used virtual work principles to model the FOAM body.

##### A. FOAM Accordion Body

We used two analytical models from the literature to predict FOAM accordion body behavior.

Gollob et al. uses a geometry-driven model, where the output force is a result of the changing internal volume; geometry (cell length, fold angle, membrane shape) is used to calculate a radial “loss volume” as the actuator compresses [10]. The paper skeleton is not modeled as a discrete spring. This approach is strong for capturing how different geometries shape the **force–contraction curve** and for comparing designs under constant pressure, but it can be harder to directly map to a specific physical actuator’s stiffness or to experimental loading conditions.

1.  $F = P \frac{dV}{ds}$   
 $F$  = force,  $P$  = pressure,  $V$  = internal volume,  $s$  = contraction
2.  $F_{act}^* = \frac{F_{act}}{F_p} = 1 - \frac{1}{D} \frac{dV}{ds}$   
 $F_{act}^*$  = scaled force,  $F_p$  = piston force,  $D$  = characteristic length,  $V_r$  = radial lost volume
3.  $f_s(s, h)(x) = -h \left(1 - \frac{x^2}{(s/2)^2}\right)$   
 $f_s$  = skin profile,  $s$  = cell length,  $h$  = sag depth,  $x$  = axial coordinate
4.  $f_b, \text{bellows}(x) = -\frac{D}{2}$   
 $f_b$  = boundary function,  $D$  = diameter
5.  $f_{b,\text{FOAM}}(L, s)(x) = 2 \frac{d}{s} |x| - d$ ,  $d = \sqrt{\left(\frac{L}{2}\right)^2 - \left(\frac{s}{2}\right)^2}$   
 $L$  = skeleton length,  $s$  = contraction,  $d$  = skeleton height,  $l_i$  = zig-zag section length
6.  $h_{i,next} = \frac{h_{i,lower} \text{dist}_{upper} + h_{i,upper} \text{dist}_{lower}}{\text{dist}_{upper} + \text{dist}_{lower}}$   
 $h$  = sag depth,  $\text{dist} = |l_s(h) - b|$ ,  $b$  = skin length

In contrast, Li et al. uses a force-balance model explicitly represents the zigzag skeleton as a **spring system** with a bending stiffness, and combines this with a pressure-driven virtual-work term to give a closed-form expression for the net output force as a function of fold angle and contraction [7]. Because it includes both pressure effects and elastic restoring forces, Li’s model is well suited for predicting how much load the actuator can support at a given contraction and for matching experimental blocked-force measurements, but it is more specialized to the zigzag geometry and relies on accurate estimates of material properties like  $E$  and wall thickness.

- $F = PA$   
 $F$  = pressure-generated axial force,  $P$  = internal pressure difference,  $A$  = end-area projection
- $k_s = \frac{EWt^3}{4D^3}$   
 $k_s$  = skeleton spring constant,  $E$  = Young's modulus,  $W$  = beam width,  $t$  = thickness,  $D$  = beam depth
- $F_e(\theta) = k_s \Delta L(\theta)$   
 $F_e$  = elastic spring force,  $\Delta L(\theta) = L_0 - L(\theta)$
- $F_{\text{output}}(\theta) = 2(F(\theta) - F_e(\theta))$   
 $F_{\text{output}}$  = net axial output,  $F(\theta)$  = pressure force,  $F_e(\theta)$  = spring resistance
- $C(\theta) = 2N(L_0 - L(\theta)) = 2N(\sin \theta_0 - \sin \theta)$   
 $C$  = total contraction,  $N$  = number of zigzag units,  $\theta_0$  = initial hinge angle
- $\gamma = \frac{C(\theta)}{L_0}$   
 $\gamma$  = contraction ratio,  $L_0$  = initial actuator length

For both models we define the contraction ratio as:

$$1. \gamma = \frac{L_0 - L}{L_0}$$

$\gamma$  = contraction ratio,  $L_0$  = initial actuator length,  $L$  = current length

Using known parameters from our robot body shown in Table [x] we emulated both models in MATLAB to simulate the force-contraction profile assuming constant-pressure. The profile in Figures X and Y represent the static force the actuator could exert if held at a given contraction while pressure is kept constant, under both the geometry-driven and force-balance models. Both simulations show that as contraction increases, mechanical advantage is reduced and force decays as the structure collapses inward. In other words, the uncontracted actuator is able to produce a high force at the beginning of the contraction. The pulling force that the actuator can still generate declines as it contracts.

Since we plan to inflate and deflate our robot using syringes and not a vacuum pump, we expect pressure to change with contraction. Using the Li force-balance model in MATLAB we simulated the pressure difference in the actuator as the body holds different weights [7]. For a given weight, a greater pressure difference is needed to achieve higher contractions to counter the increasing spring force of contraction. Additionally, higher pressure is needed to counter increasing weight at any target contraction level. These models provide a useful basis for understanding the pressure, force and contraction relationships and providing an expectation for the pressure and force output needed to handle different loads.

TABLE 1. FOAM Model Inputs

| Measurement                | Value   |
|----------------------------|---------|
| Single cell segment length | 3.23 cm |
| Width                      | 6.11 cm |
| Height                     | 1.28 cm |

|  |                      |
|--|----------------------|
| “Piston” Cross-sectional Area (Width x Height)       | 7.82 cm <sup>2</sup> |
| Cell Angle   | 38°                  |
| Pressure Difference (for constant pressure modeling) | 15 kPa               |

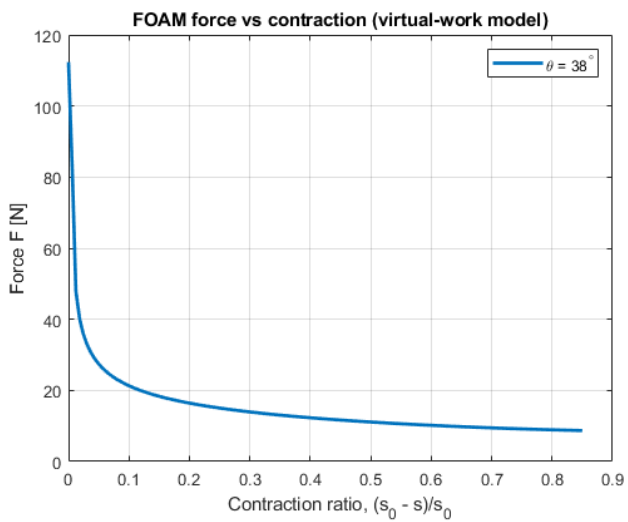


Figure []: Geometry driven virtual work model

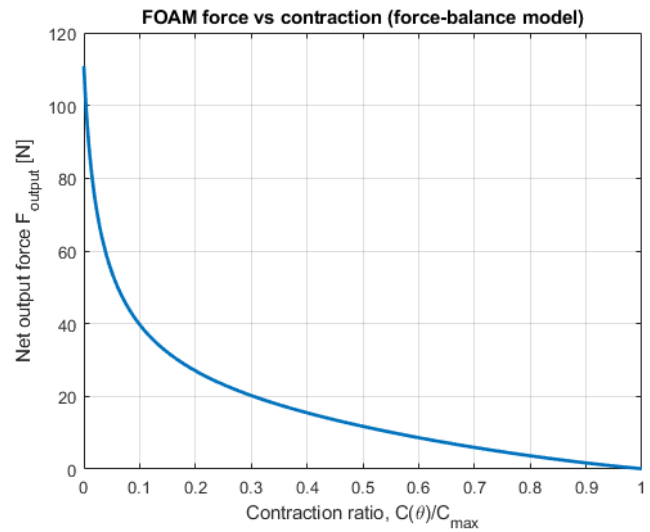


Figure []: Force-balance driven virtual work model

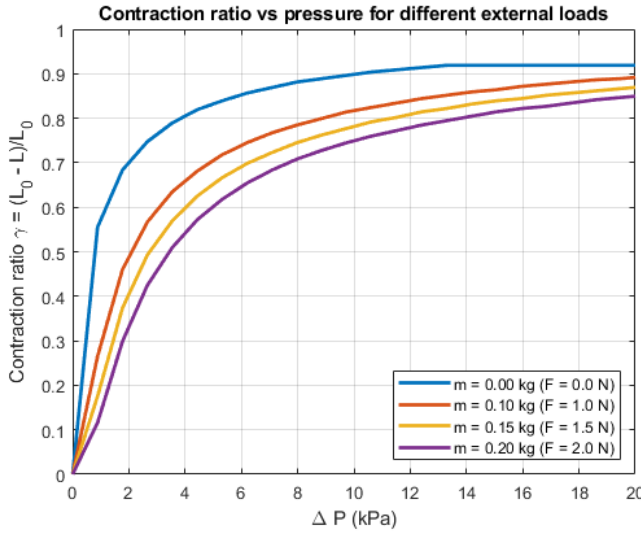


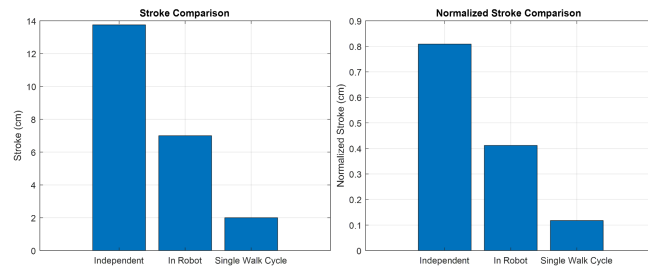
Figure []: Contraction ratio vs Pressure difference and weight

## V. TESTING & VALIDATION OF FUNCTIONALITY

We tested and characterized our fabricated robot on the following: Stroke, speed, force output of the body and feet, grasping strength, handling of different terrain types, and steering.

### A. Stroke

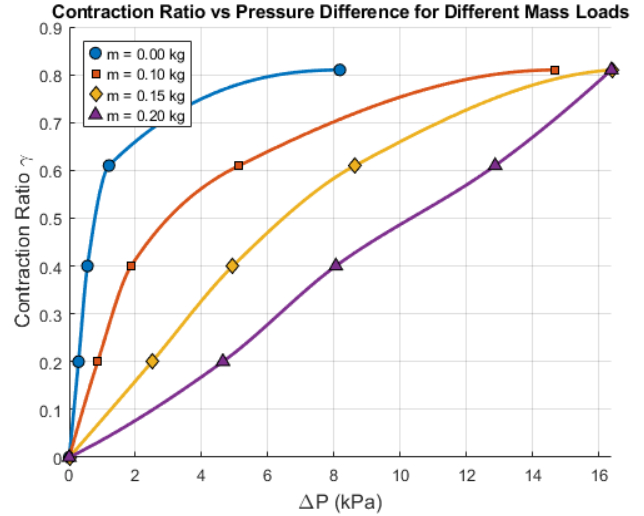
The stroke of the FOAM accordion body was characterized independently, within the robot structure, and as the overall forward movement after one full walking cycle. The results are shown below in terms of both real stroke distance and normalized stroke distance. Normalized stroke was calculated by dividing the real stroke distance by the full length of the uncontracted FOAM body.



The single walk cycle captures about 15% of the stroke potential determined by the independent FOAM body stroke. Stroke is lost due to the restriction by the stiffeners, which is captured as the loss of stroke in the robot configuration, and due to foot slip while walking. Alleviating the restrictiveness of the stiffeners and further experimentation with foot design and foot friction can improve stroke.

## B. Force Output of FOAM Accordion Body and Angular Pouch Feet

Force output was characterized as the pressure difference needed to hold up a given mass to a given displacement. The testing was conducted by securing the FOAM body vertically, adding weights of varying masses, pulling air out of the body to contract the mass to a target contraction ratio, and then recording the pressure recorded by a pressure sensor hooked up to an Arduino.



These results show that with increasing mass, a greater pressure difference is needed to achieve the same displacement. Even with no mass, some pressure is required to counter the spring-like effect of the compressed accordion. These results match the trend seen in our modeling (Figure [x]) in terms of magnitude of pressure differences and the trend of requiring greater pressure differences to displace heavier weights.

For a horizontally walking robot, these results speak to the frictional forces the robot can overcome to contract to a target level of displacement during each walk cycle. For example, 0.20 kg of mass hanging vertically translates to 1.96 N of force. Our results suggest for a horizontal robot, ~13 kPa of pressure difference would be needed to contract the body to a contraction ratio of 0.60.

### Angular Pouch Motors

To characterize the stroke behavior of the angular pouch motors, each actuator was incrementally inflated to a series of prescribed volumes, and the resulting rotation of the foot was recorded. This procedure revealed a strong linear relationship between inflation volume and angular displacement, indicating that the actuator's output motion scales proportionally with the internal volume change.

Additionally, the maximum shear of the angular pouch motors are able to resist was tested by fully deploying the foot and

connecting a string to the end of the foot and then hanging the end off the edge of the table. Weights were incrementally added to the end of the string until the foot slipped.

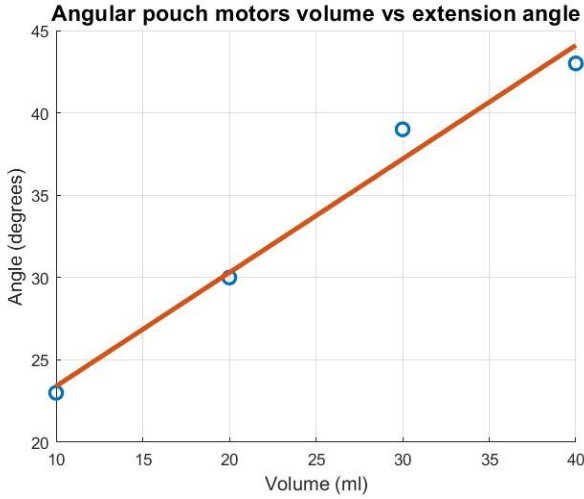


Figure [X]: Angular pouch motors volume vs extension angle.

The maximum force output of each motor was characterized by placing the PLA structure in a vice and then hanging weights off the end of the foot and then adding weights until the pouch motor can no longer lift it. The results are presented in Table [X].



Figure [X]: Angular pouch motor force test setup.

TABLE 2. Pouch motor key characteristics

|                              |      |
|------------------------------|------|
| Max weight resisted in shear | 180g |
| Max weight lifted            | 550g |
| Max Stroke                   | 50°  |

### C. Grasping Strength

The grasping mechanism generates force through two independent modes: inflation and stiffening. Each mode is capable of producing a stable grasp and was evaluated separately.



Figure [X]: shows the six molds used for characterization: from left to right, a 1" x 1" rectangular mold, 1.5" x 1.5" rectangular mold, 1" x 1" cylindrical mold, 1.5" x 1.5" cylindrical mold, 1" x 1" conical mold, and a 1.5" x 1.5" conical mold.

To assess the performance of each grasping mode, the three mold geometries, rectangular, cylindrical, and conical, were fabricated in two sizes, resulting in six total test molds. Each mold was individually weighed, and additional mass was hung from the mold's handle until the grasper could no longer maintain its hold. The maximum supported loads for each configuration are shown in Tables X and X.

TABLE 2. Maximum suspended load for each 1" x 1" mold using inflation and stiffening.

| Grasping Strength<br>1" x 1" Profile<br>Molds | Grasping Mode              |                            |
|---|----------------------------|----------------------------|
|   | Inflation                  | Stiffening                 |
| Shape   | Total Suspended Weight (g) | Total Suspended Weight (g) |
|   | Rectangular                | 242                        |
|   | Cylindrical                | 318                        |
| Cone  | 279                        | 79                         |

TABLE 3. Maximum suspended load for each 1.5"×1.5" mold using inflation and stiffening.

| Grasping Strength<br>1.5"x1.5" Profile<br>Molds | Grasping Mode              |                            |
|---|----------------------------|----------------------------|
|   | Inflation                  | Stiffening                 |
| Shape   | Total Suspended Weight (g) | Total Suspended Weight (g) |
| Rectangular                                     | 372                        | 42                         |
| Cylindrical                                     | 368                        | 28                         |
| Cone  | 509                        | 79                         |

In all cases, inflation enables the grasper to support significantly higher loads than stiffening. The cone-shaped molds consistently exhibit the highest supported weight, while the rectangular and cylindrical molds perform similarly but at lower capacities. This trend is expected: the conical geometry provides an undercut that the grasper can mechanically support, whereas the rectangular and cylindrical molds rely solely on friction. Inflation increases the normal force applied to the mold walls, increasing frictional resistance and thereby outperforming the stiffening-only mode.

#### D. Incline and Rough Terrain Handling

A wooden ramp system was constructed to evaluate the robot's performance on inclined surfaces. The robot was able to climb slopes up to 5.4°, though its speed and stroke efficiency decreased noticeably with increasing incline. At steeper grades, the main point of failure was foot slippage. The angular pouch motors could not generate sufficient normal force between the feet and the ground to maintain traction, causing the chassis to remain largely stationary. Increasing the coefficient of friction between the foot and the ground through either different geometry or materials may provide improved performance for the robot on inclined surfaces. Increasing the friction in viscoelastic materials is nontrivial, however employing methodology as described by Wei et al [11] may provide insight into materials or geometries that may improve this.

#### E. Active and Passive Steering

To evaluate active steering, the robot was operated in the stiffen-under-elongation mode. To do this, the robot was aligned with a starting baseline and actuated for three turn cycles. Its final orientation was captured, measured, and divided by the number of turn cycles to determine an average turning angle per stroke of ~4.41° (FIGURE NUMBER). Using this specification and the average walk cycle distance of 2 cm (Figure #), the

average turning radius is calculated to be ~26 cm, indicating an achievable U-turn in ~40 turn cycles and a footprint of ~0.14 m^2. This however assumes a no-slip condition. In reality, due to partial slipping of the silicone feet, some amount of forward translation is lost with each turning cycle, meaning the true turning radius is likely smaller, making the robot maneuverable in relatively tight spaces.

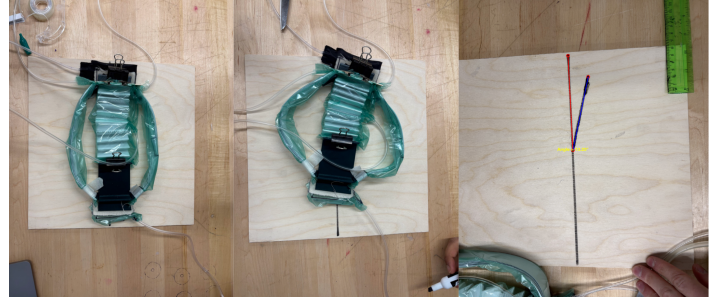
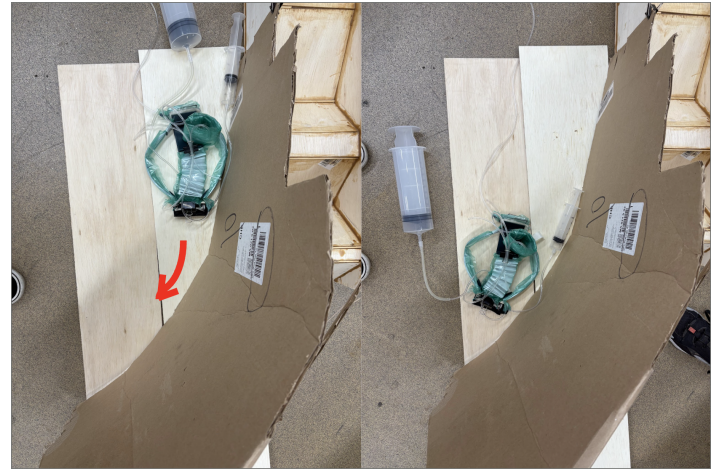


Figure # – measurement of active steering capability

Due to the innate compliance and flexibility of the actuators, namely yaw-axis bending of the FOAM and the curved bumper-like nature of the laminar stiffeners, the robot can follow gently curved interfaces, resulting in a passive steering capability. This was demonstrated using a setup of a curved cardboard wall. With no stiffening, the robot is able to follow the curve only by walking forward (FIGURE NUMBER). This morphological computation highlights the ability of the robot to interact with unpredictable environments without the need for additional actuation.



Figure# – demonstration of passive steering capability

## VI. CONCLUSION & IMPACT

Through the integration of a FOAM-inspired accordion body, deployable angular pouch-motor feet, steering stiffeners, and an inflatable grasper, we developed a soft robot capable of locomotion, steering, and object manipulation. We characterized

the performance of each subsystem and identified several design modifications that could further improve capability.

One improvement involves increasing the frictional force between the angular pouch-motor feet and the ground. Since friction is governed by both the coefficient of friction and the normal force, and increasing the normal force would likely require adding unwanted weight, our next steps focus on exploring alternative foot materials and geometries to maximize the coefficient of friction.

We also aim to refine the length of the steering stiffeners. In the current design, the stiffeners are slightly too long, causing them to buckle and expand the robot's width, which limits navigation in confined spaces. By systematically testing different stiffener lengths, we expect to identify a configuration that maintains effective steering while improving the robot's ability to maneuver through tighter environments.

In terms of broader impact, this work establishes a general robot architecture for real-world applications in industrial inspection, rubble navigation, pipeline diagnostics, and other confined or tortuous environments where rigid robots cannot safely deploy. These use cases align with documented needs in pipe-inspection and disaster-response robotics, where worm-like pneumatic anchoring and deformable bodies offer unique advantages [3].

The robot's modular actuation strategy, which pairs compliance, frictional contact, and selective stiffening, provides a blueprint for future systems that can integrate cameras, sensors, or tools for inspection and intervention tasks. By validating an inexpensive and highly adaptable soft robot capable of locomotion, steering, and manipulation, this project expands the design space for soft machines and contributes to the broader goal of creating deployable, safe, and resilient robots for challenging environments.

## VII. APPENDIX

## VIII. REFERENCES

1. A. Comoretto, H. A. H. Schomaker, and J. T. B. Overvelde, "Physical synchronization of soft self-oscillating limbs for fast and autonomous locomotion," *Science*, vol. 388, no. 6747, pp. 610–615, May 2025, doi: 10.1126/science.adr3661.
2. "A flexible robot can help emergency responders search through rubble | MIT Lincoln Laboratory," Mit.edu, 2025. <https://www.ll.mit.edu/news/flexible-robot-can-help-emergency-responders-search-through-rubbl>
3. Blewitt, G.; Cheneler, D.; Andrew, J.; Monk, S. A review of worm-like pipe inspection robots: research, trends and

challenges. *Soft Sci.* 2024, 4, 13. <http://dx.doi.org/10.20517/ss.2023.49e>

4. D. Guo, Y. Wang, and Z. Kang, "A Hollow Shell-Lattice Soft Robot in Flexible Pipelines with Flowing Fluids," *Advanced Science*, vol. 12, no. 21, Mar. 2025, doi: 10.1002/advs.202414882.

5. J. Yang, M. Runciman, J. Avery, Z. Sun, and G. Mylonas, "A Soft Inflatable Robot Driven by Hydraulic Folded Pouch Actuators for Minimally Invasive Surgery," *IEEE Robot. Autom. Lett.*, vol. 9, no. 5, pp. 4870–4877, May 2024, doi: 10.1109/lra.2024.3386022

6. Y. Wang, Z. Xie, H. Huang, and X. Liang, "Pioneering healthcare with soft robotic devices: A review," *Smart Medicine*, vol. 3, no. 1, Feb. 2024, doi: 10.1002/smmd.20230045.

7. Li, S., Vogt, D. M., Rus, D. & Wood, R. J. Fluid-driven origami-inspired artificial muscles. *Proc. Natl. Acad. Sci.* 201713450 (2017). doi:10.1073/pnas.1713450114319650.

8. Y. S. Narang, J. J. Vlassak, and R. D. Howe, "Mechanically Versatile Soft Machines through Laminar Jamming," vol. 28, no. 17, pp. 1707136–1707136, Apr. 2018, doi: <https://doi.org/10.1002/adfm.201707136>.

9. C. Chen, D. Fan, H. Ren and H. Wang, "Comprehensive Model of Laminar Jamming Variable Stiffness Driven by Electrostatic Adhesion," in *IEEE/ASME Transactions on Mechatronics*, vol. 29, no. 3, pp. 1670-1679, June 2024, doi: 10.1109/TMECH.2023.3

10. S. D. Gollob, C. Park, B. H. B. Koo, and E. T. Roche, "A Modular Geometrical Framework for Modelling the Force-Contraction Profile of Vacuum-Powered Soft Actuators," *Front. Robot. AI*, vol. 8, Mar. 2021, doi: 10.3389/frobt.2021.606938.

11. H. Wei, W. Fang, S. Wang, Z. Wang, Z. Lin, and B. Liao, "Characterizing friction coefficients of soft materials via stick-slip data in static friction: Mechanism analysis and experimental validation," *Mechanics of Materials*, vol. 213, p. 105545, 2026. doi: 10.1016/j.mechmat.2025.105545.

